

# DEEPC4: Deep Conditional Census-Constrained Clustering for Large-scale Multitask Spatial Disaggregation of Urban Morphology

Joshua Dimasaka<sup>a,b,\*</sup>, Christian Geiß<sup>c,d</sup>, Emily So<sup>a,b</sup>

<sup>a</sup>Department of Architecture, University of Cambridge, Cambridge, United Kingdom

<sup>b</sup>Cambridge University Centre for Risk in the Built Environment, Cambridge, United Kingdom

<sup>c</sup>Earth Observation Center, German Aerospace Center, Weßling, Germany

<sup>d</sup>Institute of Geography, University of Bonn, Bonn, Germany

## Abstract

To understand our global progress for sustainable development and disaster risk reduction in many developing economies, two recent major initiatives – the Uniform African Exposure Dataset of the Global Earthquake Model (GEM) Foundation and the Modelling Exposure through Earth Observation Routines (METEOR) Project – implemented classical spatial disaggregation techniques to generate large-scale mapping of urban morphology using the information from various satellite imagery and its derivatives, geospatial datasets of the built environment, and subnational census statistics. However, the local discrepancy with well-validated census statistics and the propagated model uncertainties remain a challenge in such coarse-to-fine-grained mapping problems, specifically constrained by weak and conditional label supervision. Therefore, we present Deep Conditional Census-Constrained Clustering (DEEPC4), a novel deep learning-based spatial disaggregation approach that incorporates local census statistics as cluster-level constraints while considering multiple conditional label relationships in a joint multitask learning of the patterns of satellite imagery. To demonstrate, compared to GEM and METEOR, we enhanced the quality of Rwandan maps of urban morphology, specifically building exposure and physical vulnerability, at the third-level administrative unit from the 2022 census. As the world approaches the conclusion of many global frameworks in 2030, our work offers a new deep learning-based mapping technique that explicitly encodes well-validated census and experts' belief systems to achieve an explainable and interpretable auditing of existing coarse-grained derived information at large scales.

**Keywords:** urban morphology, building exposure, physical vulnerability, spatial disaggregation, deep clustering

## 1. Introduction

As one of the key priorities of the 2015-2030 Sendai Framework for Disaster Risk Reduction (United Nations (UN), 2015) alongside the targets of the 2030 Agenda for Sustainable Development (UN, 2015), the need to understand disaster risk at large scales has urged recent various multi-country projects such as the METEOR project for UN-designated Least Developed Countries (LDCs) (Huyck et al., 2019) and the Global Earthquake Model (GEM) Foundation Uniform Africa Exposure Data (Paul et al., 2022) to map the locations of populated human settlements and buildings in many developing economies. Assessing disaster risk complements this information on the exposed location with the characterization of physical vulnerability, which is commonly described in terms of the type of construction material and the height of a building. For example, the standard taxonomies of GEM (Brzev et al., 2013), PAGES-STR (Jaiswal et al., 2010), HAZUS (Kircher et al., 2006), and EMS-98 (Grünthal, 1998) provide a classification system on building typologies, indicating the inherent structural capacity or vulnerability of a building. More broadly, in a regional scale, this

characterization of the physical attributes of buildings collectively contributes to the three-dimensional urban form or morphology of a place (Labetski et al., 2023).

However, while such large-scale efforts using classical spatial disaggregation techniques have revealed a comprehensive understanding of the urban morphology indicators used for regional disaster risk assessment, its numerical discrepancy with well-validated census records at the local level has remained a significant challenge in establishing a general consensus between the data-driven mapping techniques and the local knowledge and practice (Wardrop et al., 2018; Petrarulo et al., 2022), thereby limiting its use by the wider community such as urban planners and disaster risk managers on the ground (Gevaert et al., 2021). Although other finer-grained efforts such as building-level attribute identification have shown reliable predictive performances (Geiß et al., 2018; Gouveia et al., 2024; Silva et al., 2024), these alternatives are data-expensive, resource-intensive, and scope-limited, when scaling up to a larger areal extent. Thus, the tradeoff between the resolution quality of mapping and the accuracy of information has become a primary issue in supporting the evidence-based decisions of many global frameworks (Clark et al., 2023).

Despite the potential wide-scale offerings of previous

\*Corresponding Author: jtd33@cam.ac.uk

studies, their use of secondary products and input satellite imagery with varying temporal signatures further compounded and propagated the spatial uncertainties of the resulting maps of urban morphology indicators. For example, even though both GEM and METEOR used the rich information from remote sensing data and the data-driven techniques such as the random forest tool (Stevens et al., 2015) for WorldPop population map (Tatem, 2017) and the symbolic machine learning (Blei et al., 2018) for Global Human Settlement Layer (Pesaresi et al., 2024), the performance of WorldPop for Kenya still achieved 60% (Stevens et al., 2015). In addition, the METEOR project used varying temporal information of their input geospatial maps due to the unavailability of temporally coherent data during the time of analysis (Huyck et al., 2019). As a result, these challenges inherent to the model uncertainties still necessitate subsequent careful validation and other independent analyses for suitability and overall quality (Gevaert et al., 2021).

Nevertheless, the increasing availability of public EO data and acquisition platforms such as Google Earth Engine (Gorelick et al., 2017) has recently enabled many new opportunities and improvements in various geospatial modelling of direct and indirect indicators of urban morphology such as the spatial disaggregation of building energy consumption (Zhou et al., 2023), population (Darin et al., 2022), building material type using height distribution (Geiß et al., 2023), and settlement structure characteristics (Meinel et al., 2009). While such region-specific examples have demonstrated the simplicity and flexibility in dealing with the non-uniform, highly diverse, and heterogeneous classifications at large scales, the quality of the coarse-to-fine-grained disaggregation task remains weakly supervised. For example, a particular building height category can correspond to multiple possible classifications of wall and roof material, thereby introducing multiple one-to-many, many-to-many, or fuzzy combinations (Pittore et al., 2018; Gómez Zapata et al., 2022). Specifically, a residential wooden building has 40-75%, 25-40%, and 0-20% chances to have one, two, and three storeys, respectively, according to the outcomes of the SSAHARA survey of the expert belief system on the local indigenous knowledge of construction practice (Paul et al., 2022). Because of the limited generalizability due to the weak and conditional supervision, numerous studies have similarly implemented deep constrained clustering techniques in renewable electricity modelling (Seljom et al., 2021) and agricultural crop management (Lampert et al., 2019; Lafabrègue and Gançarski, 2025) to extend the model capability on high-dimensionality and non-linearity of EO data, with the consideration of coarse-grained label information as cluster-level constraints that can provide performance guarantee (Bradley et al., 2000; Wagstaff et al., 2001; Demiriz et al., 2008; Zhu et al., 2010).

Therefore, we develop the Deep Conditional Census Constrained Clustering (DeepC4), a novel deep learning-based spatial disaggregation approach that fundamentally addresses the numerical discrepancy with coarse-grained or cluster-level labels (e.g., census statistics) and incorporates conditionality

on multiple possible labels (i.e., from experts' belief system gained from local indigenous knowledge) in a multitask optimization, while still exploiting the richness of information that can be derived from near-real-time publicly available satellite imagery and other derived products. This coarse-to-fine-grained approach can also be generalizable to other weakly supervised problems that involve the use of EO data for urban informatics applications with encoded constraints from other external validation surveys. By considering the explicit importance of well-validated census and experts' belief systems, our approach also contributes to the overall consistency of resulting deep learning-based maps, thereby improving their relative explainability and interpretability with respect to the current understanding of end users. In this study, we demonstrate the application of DeepC4 using the case of Rwanda, one of the LDCs which has experienced a significant technological difficulty in advancing exposure mapping and its physical vulnerability characteristics.

The remainder of this paper is organized as follows: Section 2 details the information about census statistics, expert belief systems on the conditional relationships of urban morphology, satellite imagery, and built-area datasets. Section 3 describes the preprocessing steps, the iterative construction of a probable space of building presence for disaggregation implementation, and the DeepC4 algorithms on dimensional reduction and joint multitask learning optimization. Section 4 compares our findings with the corresponding outputs of the METEOR project and the GEM for the entire Rwanda and explains the numerical evaluations of the performance of DeepC4 in achieving learning stability while minimizing the errors in the clustering implementation.

## 2. Materials

### 2.1. Study Area

With over 26,300 square kilometers and located in the east-central region of the African continent, the densely populated country of Rwanda consists of 416 sectors, 30 districts, and 5 provinces, as shown in Figure 1.

### 2.2. Census Statistics

From the Fifth Population and Housing Census (RPHC5) 2022 with acceptable data quality at a net coverage rate of 98.7% and a rate of erroneous inclusion of 0.2% (National Institute of Statistics Rwanda, 2023), we used the sector-level census statistics as cluster-level constraints to DeepC4. Specifically, we obtained 416 rows of data on average household size, urban and rural population counts, 14 wall material classes, and 9 roof material classes.

For the year 2022, the average household size ranged from 3.05 up to the highest value of 5.46 population per household unit that was achieved by Nkombo, Rusizi, Western Province. The least and most populated sectors were Gitovu, Burera, Northern Province at 11,531, and Kinyinya, Gasabo, Kigali City at 125,400, respectively. Across all sectors, the most

frequent wall and roof materials were sun-dried bricks and iron sheets, respectively.

At the national scale, (Paul et al., 2022) reported that only 1.4% and 0.6% respectively correspond to the commercial and industrial occupancies of the 2020 building counts, whereas the majority at 98% is residential. Hence, we further assumed that our study is primarily concerned with the number of residential buildings with minimal underestimation effect on the overall results at the sectoral level.

### 2.3. Experts' Belief System on Construction Practice

We considered the valuable encoded mapping scheme of Paul et al. (2022), which creates discrete probabilistic relationships among wall material, height, and macro-taxonomy classes, since it is based on a comprehensive engagement and judgment of local experts on the construction methodology. This information controls the learning behavior of DeepC4 using the numerical conditions among these urban morphology indicators. As presented in Appendix A, this explicit encoding of discrete conditional probability values supports the interpretability of resulting maps since the inferred distribution of classes, including any deviations, can be explained by the probabilistic relationships.

Table 1 enumerates the complete list of urban morphology indicators in our resulting Rwandan maps, which were reduced from the original literature (Paul et al., 2022) due to the overlapping general characteristics and additional computational benefit in the implementation of constrained clustering (i.e., lower number of categories results in less computational demand). However, it is important to note that,

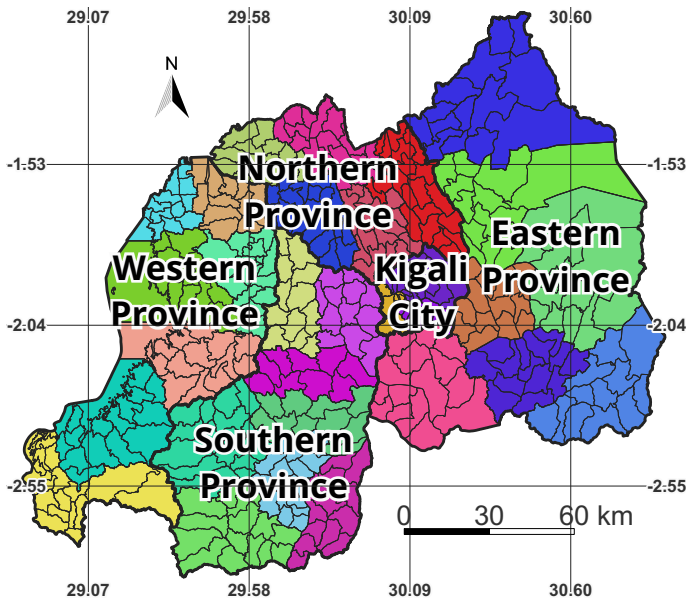


Figure 1: Geographical extent of Rwanda (Global Administrative Areas, 2022). The boundaries of sectors and provinces are respectively displayed with thinner and thicker lines. Every distinct color represents a district.

in this study, these presented indicators are limited only to physical building-level attributes, but still contribute to the understanding of the urban morphology of a place (e.g., spatial patterns, density, and other numerical metrics).

### 2.4. Earth Observation Data

We obtained the following pre-processed 10-meter satellite imagery whose signals serve as a proxy to infer the distribution of distinct urban morphology indicators for the 2022 period via Google Earth Engine (Gorelick et al., 2017). Although no experiment was performed to evaluate the marginal contribution of each signal band, our study relied on the inherent capabilities of each modality to capture relevant remotely sensed information and to primarily demonstrate the latent reduced representation for a deep constrained clustering implementation.

**Sentinel-1 SAR GRD.** Using its cloud-penetrating capability for surface roughness sensitivity (Koppel et al., 2017), we used the mean of the Ground Range Detected (GRD) scenes acquired from the dual-polarization C-band Synthetic Aperture Radar (SAR) instrument at 5.405 GHz of the Sentinel-1 satellite (Copernicus Sentinel data, 2024b). It consists of two bands: VV (vertical transmit, vertical receive) and VH (vertical transmit, horizontal receive) signals. To avoid data incompleteness across large areas, we disregarded filtering by orbital number and satellite direction.

**Sentinel-2 Harmonized MSI.** Using its multispectral imaging capability for optical signatures (Braun et al., 2019), we also extracted the median of the atmospherically corrected surface reflectance signals represented by 10 bands – red (B4), green (B3), blue (B2), red edge 1 (B5), red edge 2 (B6), red edge 3 (B7), red edge 4 (B8A), near infrared (B8), short-wave infrared 1 (B11), and short-wave infrared 2 (B12) – that are acquired from the MultiSpectral Instrument (MSI) of the Sentinel-2 satellite (Copernicus Sentinel data, 2024a). The aggregation by year also enables minimizing the unnecessary noisy cloudy or shadowy signals using the available and corresponding Sentinel-2 cloud probability dataset (Copernicus Sentinel data, 2024c).

### 2.5. Built Area Information

Given a large areal extent with several land cover types, information about the locations of built areas such as building footprints refines the number of potential locations to be assigned with the previously mentioned urban morphology indicators. Despite the growing efforts in mapping building footprints for multi-year periods, temporally disaggregated building footprints by year remain scarce due to the limited and expensive year-specific groundtruth labels. Thus, we performed an iterative construction of possible space of disaggregated locations of building presence for the year 2022 using a combination of various imperfect building footprint datasets – OpenStreetMap (Geofabrik GmbH and OpenStreetMap Contributors, 2018), Google Open Buildings V3 (Sirko et al., 2021), Microsoft Building Footprints (Microsoft, 2024), and Overture Foundation Building

Table 1: Urban morphology indicators and their respective classes and descriptions in the resulting Rwandan maps.

Indicator	Number	Classes
Roof	4	Iron Sheets; Local, Industrial, and Asbestos Tiles; Concrete; Grass
Wall	8	Wood with mud; Sun-dried bricks; Cement bricks; Burnt bricks; Stones; Concrete; Timber; Others
Height	6	H:1 (1 storey); H:2 (2 storeys); H:3 (3 storeys) HBET:3-6 (3-6 storeys); HBET:4-6 (4-6 storeys); HBET:8+ (8 or more storeys)
Macro Taxonomy	16	CR/LFINF (reinforced concrete with infill walls)
		CR/LWAL (reinforced concrete with shear walls)
		MATO (others such as reeds, plastics, and fabrics)
		MCF+CB/LWAL (confined concrete block masonry with shear walls)
		MCF+CL/LWAL (confined clay brick masonry with shear walls)
		MUR+ADO+MOC/LWAL (unreinforced adobe block masonry with cement mortar and shear walls)
		MUR+ADO/LWAL (unreinforced adobe block masonry with shear walls)
		MUR+CB/LWAL (unreinforced concrete block masonry with shear walls)
		MUR+CL+MOC/LWAL (unreinforced clay brick masonry with cement mortar and shear walls)
		MUR+CL/LWAL (unreinforced clay brick masonry with shear walls)
		MUR+STDRE+MOC/LWAL (unreinforced dressed stone masonry with cement mortar and shear walls)
		MUR+STDRE/LWAL (unreinforced dressed stone masonry with shear walls)
		MUR+STRUB+MOC/LWAL (unreinforced rubble stone masonry with cement mortar and shear walls)
		MUR+STRUB/LWAL (unreinforced rubble stone masonry with shear walls)
		W+WWD/LWAL (wattle and daub with shear walls)
		W/LWAL (wood with shear walls)

Footprints (Overture Maps Foundation, 2023) – and the 2022 map of average probability of complete coverage by built area from the Dynamic World V1 dataset, which is a near-real-time land cover map derived from Sentinel-2 satellite imagery (Brown et al., 2022).

In our study, while it may be desirable to develop our own data-driven model to independently extract 2022 building footprints directly from EO data in our problem setting, we note that this entails the acquisition of reliable building groundtruth labels for the particular year. In contrast, because of its limited availability, we instead relied on the multi-year building footprints from these various sources and iteratively constructed a set of probable map locations (i.e., pixels) with the aid of the Dynamic World V1 dataset, which has a higher temporal resolution that enables a reliable representation for the year 2022. This iterative procedure addressing this data limitation is further discussed in Section 3.2. Nevertheless, this approach remains valid for the demonstration of DeepC4, which focuses on the deep representation and constrained clustering.

### 2.6. Building-level Groundtruth Information

While a vanilla unsupervised clustering does not necessitate any groundtruth information, our DeepC4, however, involves the training of deep neural network parameters to learn a more meaningful latent reduced representation of EO satellite imagery signals using building-level groundtruth information, which effectively supervises the constrained clustering. Because such groundtruth information in a form of a 2022 Rwandan building footprint is not widely available and may often use a different modality (e.g., different classification system), we instead used the weak and limited supervision provided by the 2015 dataset on building typology for the

Kigali City, Rwanda, which covers 30 (7.2%) out of all 416 sectors (Bachofer et al., 2019).

As a limitation, our empirical results assumed that the 2015 groundtruth information has a minimal difference with the 2022 true information by defining a common subset of map locations with valid pairs of the post-processed 2015 groundtruth information and DeepC4 2022 predictions, as presented with further details in Section 3.3.5. This implies that any subsequent interpretations are contextually limited by the geographic and temporal biases inherent in using only the available supervising information from Kigali City, Rwanda, thereby potentially disregarding distinct urban-rural differences. Nonetheless, while it may be desirable to have representative samples across the country of Rwanda, our demonstration recognizes that this current data gap reflects an important domain challenge and presents an opportunity for future fine-tuning improvement, when a large-scale survey of Rwandan building typology becomes available.

## 3. Methods

In this section, we present a detailed summary of the major procedures from the preprocessing of census information into conditional constraints and the selection of disaggregated locations of building presence using various available datasets to the implementation of our proposed DeepC4, which consists of five sections on normalization, dimensional reduction, constrained clustering, joint multitask learning, and performance evaluation, as illustrated in Figure 2.

### 3.1. Preprocessing of constraints and conditions

The preprocessing started with the encoding of census statistics from 30 district-level reports into a machine-readable

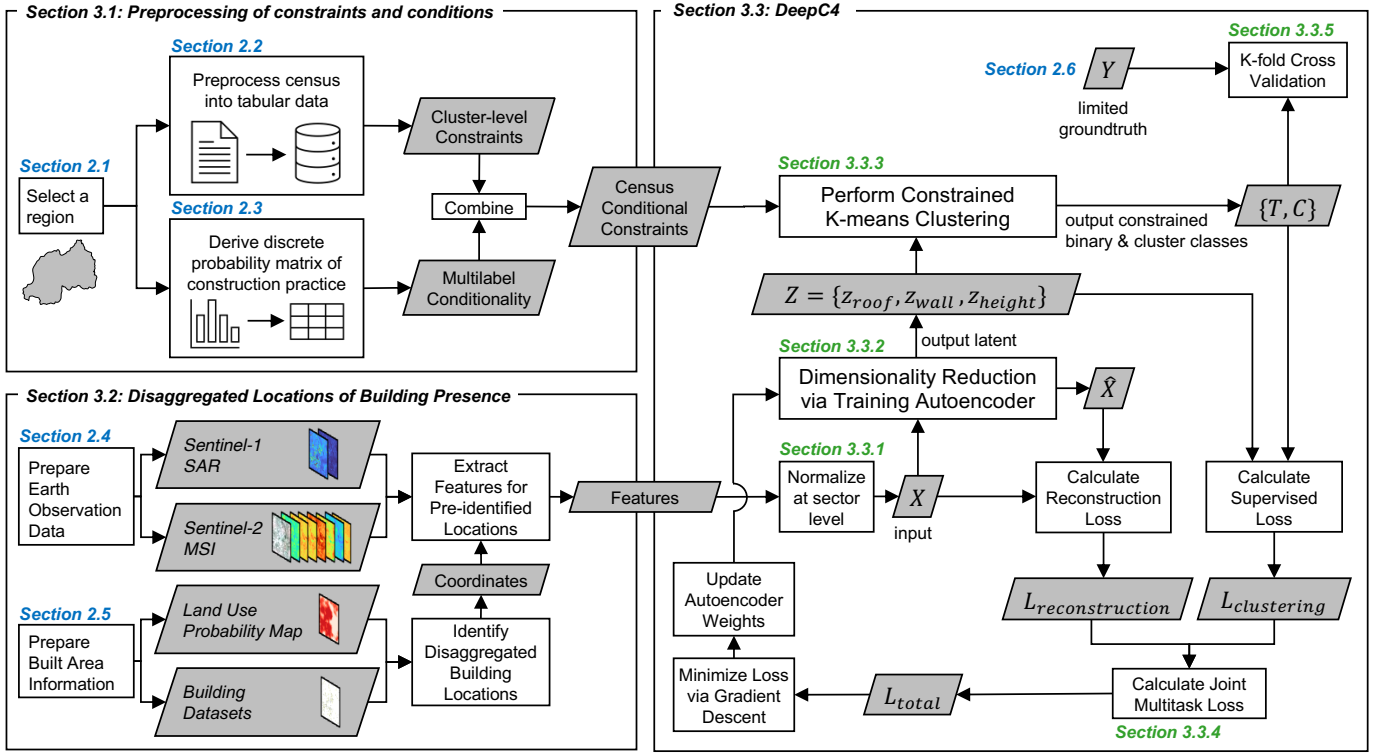


Figure 2: DeepC4 Implementation. From left to right, we began with the encoding of census conditional constraints, preparations of EO features, and selection of disaggregated building locations from various imperfect sources. We then trained an autoencoder to obtain a set of reduced-dimension latent representations that were used for constrained clustering algorithms. Jointly trained using the reconstruction and prediction losses, we evaluated the performance of the autoencoder using the available building-level groundtruth.

format. For every sector  $s_i$ , where  $i = 1, 2, \dots, N_s$  and  $N_s$  correspond to the total number of sectors in the country, we computed its corresponding average household size,  $h_{s_i}$ , by taking the ratio of sector-level population and private household count. Because the census also reported the composition of the population by urban and rural areas, we then computed the number of dwellings for urban ( $d_{s_i,urban}$ ) and rural ( $d_{s_i,rural}$ ) by respectively dividing the urban and rural population by  $h_{s_i}$ . By respective conditional proportions, we distributed  $d_{s_i,urban}$  and  $d_{s_i,rural}$  into wall, material, height, and macro-taxonomy classes using the probabilistic relationships in Appendix A. As a result, for both rural and urban areas of sector  $s_i$ , we obtained the number of buildings for each urban morphology indicator in Table 1.

However, due to the lack of temporally consistent data on building footprints in a vectorized or polygonal format, as previously discussed in Section 2.5, we transformed the building counts by approximating their equivalents to the rasterized, image, or pixel-based representation. We note that this approach may be sensitive to the vector-to-raster conversion because of the differences between the grid configuration and the orientation and geometry of the enclosed building footprints.

Thus, to enable a coherent rasterized analysis, by using a hard assumption wherein a building has a 60-m<sup>2</sup> ground floor

area similar to Paul et al. (2022), we converted the number of buildings into the number of grid pixels at 10-m scale, which is the representative spatial resolution of our EO satellite imagery signals. This follows that a 10-m grid pixel on the map, whose area is 100 m<sup>2</sup>, contains approximately 1.67 units of 60-m<sup>2</sup> buildings (i.e., 100 m<sup>2</sup> per grid / 60 m<sup>2</sup> per building). We used the resulting number of grid pixels as our transformed constraints in the succeeding section. When high-resolution imagery becomes available, it follows that this approximating assumption can remain valid, with further reduced uncertainty brought about by the sensitivity to vector-to-raster conversion.

### 3.2. Disaggregated locations of building presence

Due to the imperfect nature of our built area information, for every sector  $s_i$ , we iteratively constructed a set of possible grid pixels that could represent building presence. The overall procedure mainly relies on determining a threshold between 0 and 1 that interacts with the 2022 map of average probability of complete coverage by building area from the Dynamic World V1 dataset (Brown et al., 2022) until the number of grid pixels, ( $n_{constraint}$ ), at a particular threshold matches the transformed cluster-level constraints (i.e., the required number of grid pixels).

Using the rasterized footprints from the combined four building datasets within the geographical extent of sector  $s_i$ ,

we first obtained the number of grid pixels with rasterized building footprint signals ( $n_{bldg}$ ) and then evaluated its difference from the expected number of buildings that was previously calculated from the transformed constraints. If  $n_{bldg}$  did not exceed  $n_{constraint}$ , we obtained additional grid pixels to match  $n_{constraint}$ . Using the 2022 map of average probability of complete coverage by building area, we gradually decreased the probability threshold starting from the largest probability associated with  $n_{bldg}$  until the difference became negligible. Similarly, if  $n_{bldg}$  was more than  $n_{constraint}$ , we removed excess grid pixels to match  $n_{constraint}$  by gradually increasing the probability threshold starting from the smallest probability associated with  $n_{bldg}$  until the difference also became negligible. Using the calculated probability threshold, we prepared the final set of valid grid pixels with  $M$  distinct locations that DeepC4 used to construct the feature array of EO satellite imagery signals.

### 3.3. DeepC4

Unlike the two previous sections, which are applied to all 416 sectors, the succeeding sections on the implementation of DeepC4 relied on only 20 sectors with available building-level groundtruth information, which are all primarily located within and near the most populous province of Kigali City.

#### 3.3.1. Sector-level normalization

For every sector  $s_i$  of the 20 sectors, to achieve a properly scaled feature array as input to our DeepC4, we normalized the logarithm of each EO satellite imagery band (e.g., red or B4) across all  $M_i$  distinct locations with zero mean and one standard deviation. For location encoding, we also normalized the row and column indices of its grid pixels. Thus, we prepared a feature array,  $X_{s_i} \in \mathbb{R}^{|M_i| \times 14}$ , with varying first dimension, which depends on the size of  $M_i$  distinct locations, and a fixed 14 columns corresponding to the number of EO satellite imagery signals including the two location encoding features. This resulted in a combination of 127,757 grid pixels across all 20 sectors.

#### 3.3.2. Dimensional reduction

For computational efficiency and consistency of constrained clustering implementation, we extracted a low-dimension latent representation,  $Z_{s_i}$ , from the high dimensionality of  $X_{s_i}$  using an autoencoder, a deep non-linear reduction technique. While the use of other image-based deep learning techniques may be desirable to capture spatial or positional information, these approaches require an approximate transformation of cluster-level constraints into corresponding image tiles. The autoencoder addressed this limitation by incorporating  $X_{s_i}$  with location encoding features in a tabular format, as the cluster-level constraints are only expressed at the sector level and not in a form suitable for image tile representation.

Following a fully connected layer network architecture, our study assigned an arbitrary number of latent channels to each urban morphology indicator, as shown in Figure 2. In this study, we used a total of three latent channels for roof ( $z_{s_i,roof}$ ),

wall ( $z_{s_i,wall}$ ), and height ( $z_{s_i,height}$ ) in such a way that each separate latent channel is correspondingly interpretable to individual urban morphology indicator. Across all 20 sectors, we trained a single set of deep neural network parameters until the model performance converged, indicating that the learned latent representation has achieved a desirable clustering behavior given the conditional constraints under consideration.

Using the adaptive moment estimation (Adam) algorithm (Kingma, 2014) at a learning rate of 0.0001, a square gradient decay factor of 0.95, and a gradient decay factor of 0.80, we evaluated the autoencoder reconstruction loss in terms of mean-squared error (MSE), which is calculated for every sector  $s_i$  (see Equation 1), and combined it for joint optimization with the calculated loss from the constrained clustering in the succeeding section.

$$L_{s_i,reconstruction} = \frac{1}{|M_i|} \sum_{j=1}^{|M_i|} (x_j - \hat{x}_j)^2 \quad (1)$$

where  $x_j$  is the  $j^{th}$  element of the sector-level normalized feature array  $X_{s_i}$  with size  $|M_i|$  grid pixels and  $\hat{x}_j$  is its corresponding reconstruction.

#### 3.3.3. Constrained clustering

Prior to the clustering implementation, we processed the building-level groundtruth information because the building typology classification of Bachofer et al. (2019) (e.g., building height as a continuous variable) is different from the classes of every urban morphology indicator presented in Table 1 (e.g., building height as a discrete and overlapping variable). Upon inspection, we created a mapping scheme to match their respective shared and overlapping characteristics, as presented in Appendix B. Similar to the fuzzy scoring approach of Pittore et al. (2018), such assumptions are necessary, particularly in the limited and weak supervision setting of this domain problem, to demonstrate the implementation of DeepC4, thereby generalizing for cases with more precise building-level groundtruth information as it becomes available.

The DeepC4 extended the constrained k-means clustering algorithm developed by Bradley et al. (2000) with the low-dimension latent representation learning to exploit the rich information of EO data using deep and flexible neural networks and the joint multitask learning across three urban morphology indicators, resulting in a k-means-friendly space with optimal and stable clustering behavior that is weakly supervised by conditional constraints and available building groundtruth information.

Following the mathematical formulation of Bradley et al. (2000) and modifying it into the context of our study, DeepC4 implements that, for every sector  $s_i$  with corresponding latent representation  $Z_{s_i} = \{z_{s_i,roof}^j, z_{s_i,wall}^j, z_{s_i,height}^j\}_{j=1}^{|M_i|}$  with size of  $|M_i|$  grid pixels, we determined the optimal  $k$  target cluster centers  $C_{s_i}^1, C_{s_i}^2, \dots, C_{s_i}^k$  with minimized sum of the 2-norm distance squared between each  $j^{th}$  point of  $Z_{s_i}$  and its set of nearest cluster center  $C_{s_i}^h = \{c_{s_i,roof}^h, c_{s_i,wall}^h, c_{s_i,height}^h\}_{h=1}^k$ . In symbols,

$$\min_{C_{s_i^1, \dots, C_{s_i^k}}^k} \sum_{j=1}^{|M_i|} \min_{h=1, \dots, k} \left( \frac{1}{2} \|Z_{s_i} - C_{s_i}^h\|_2^2 \right) \quad (2)$$

Reframing Equation 2 with the use of a binary selection array  $T_{j,h} \in \mathbb{R}^{|M_i| \times k}$  (i.e.,  $T_{j,h} = 1$  if, for example, the latent representation  $z_{s_i,roof}^j$  is closest to center  $c_{s_i,roof}^h$  and zero otherwise) gives:

$$\begin{aligned} & \underset{C, T}{\text{minimize}} && \sum_{j=1}^{|M_i|} \sum_{h=1}^k T_{j,h} \cdot \left( \frac{1}{2} \|Z_{s_i} - C_{s_i}^h\|_2^2 \right) \\ & \text{subject to} && \sum_{h=1}^k T_{j,h} = 1, j = 1, \dots, |M_i| \\ & && T_{j,h} \in \{0, 1\}, j = 1, \dots, m, h = 1, \dots, k \end{aligned} \quad (3)$$

Iteratively solving for  $T_{j,h}$  given fixed  $C_{s_i}^h$  (i.e., cluster assignment) followed by computing the  $C_{s_i}^h$  given fixed  $T_{j,h}$  (i.e., cluster update) achieves the optimal values for  $T_{j,h}$  until the changes in  $C_{s_i}^h$  become negligible.

The DeepC4 considered the conditional constraints as input to the minimum cost network flow optimization algorithm (Bradley et al., 2000) via integer linear programming (Huangfu and Hall, 2018) as an equivalent formulation. For example, if each of 1,000 grid pixels has a directed connection to every possible cluster assignment (e.g.,  $N$  number of roof classes), resulting in an exhaustive network with  $N \times 1000$  candidate connections. In this way, the ‘flow’ signifies a selected cluster to which a particular grid pixel will be assigned. Assuming a uniform cost to trigger ‘flow’ or ‘cluster selection’ for every connection between any grid pixel and the chosen cluster, our objective is to achieve a minimum cost in such a way that the total ‘flow’ to each possible cluster should follow the provided conditional constraints in the beginning because the total ‘flow’ refers to the desired minimum number of grid pixels for each possible cluster assignment, as presented in Table 1.

Using Equation 4, we computed a Euclidean distance-based supervised loss using the final assignments for cluster  $C_{s_i}^h$ , learned latent representation, and building-level groundtruth information for each urban morphology indicator.

$$L_{s_i, clustering} = w_{label} \sum_{j=1}^{|M_i|} \left[ T_{j,h} \sqrt{(Z_{s_i} - C_{s_i}^h)^2} \right] \quad (4)$$

where  $w_{label}$  is a vector of weighting factors, proportionally accounting for the imbalanced number of overlapping cluster assignments for each label, which sums up to unity.

### 3.3.4. Joint multitask learning

It is important to note that, while the clustering is separately convex-optimizing to find its centers, it still depends on the learned latent representations as a direct result of the training of our autoencoder neural network. This joint minimization of the reconstruction loss (Equation 1) and the clustering loss (Equation 4) influencing a number of latent representations (i.e., of multiple urban morphology indicators) effectively results in a joint multitask learning. In this study, we calculated the joint total loss (Equation 5) as unweighted because our initial training implementation suggested

comparable orders of loss magnitude while considering the differences in the discreteness of latent labels and the continuous nature of reconstructed signals.

$$L_{s_i, total} = L_{s_i, clustering} + L_{s_i, reconstruction} \quad (5)$$

### 3.3.5. Performance evaluation

While clustering is an unsupervised approach, the use of deep representation learning in the form of autoencoder neural networks to infer cluster assignments still requires validation to evaluate the resulting trained autoencoder. Due to the limited sample of 20 sectors only, we performed a five-fold cross-validation wherein we set four sectors for each fold (i.e., 20 sectors  $\div$  5 folds). For five times, we tested and averaged the performance of every model trained using only 16 remaining sectors on each unseen fold with six randomly selected sectors.

In addition, the overlapping characteristics of labels (i.e., many-to-many mapping) between Bachofer et al. (2019) ( $Y_{Ch}$ ) and the target classes ( $C_{s_i}^h$ ) present a difficulty in using standard accuracy metrics, accounting for shared characteristics of the classes of each urban morphology indicator. The task of assigning binary classification metrics has become complicated (i.e., ambiguous or ill-defined negatives) due to the weak and limited supervision of the available building groundtruth information in a multiclass context. Nonetheless, the validity of predictions can still be conservatively verified against the three derived mapping tables in Appendix B. Thus, we reported the performance of our resulting trained DeepC4 model using the proportion of valid predictions (Equation 6) with multiple OR operators, which measures the fraction of predictions that satisfy these limitations of label ambiguity. This simplifies the performance evaluation of whether the trained DeepC4 model results in a valid (i.e., with a check symbol in the mapping table) or invalid (i.e., otherwise) prediction.

$$p_{valid} = \frac{\sum X}{|M_i|} \quad (6)$$

where  $|M_i|$  indicate the number of grid pixels and:

$$X = \begin{cases} 1, & \text{if } C_{s_i}^h \in Y_{Ch} \\ 0, & \text{otherwise} \end{cases}$$

Equally important to the selection of the final trained model is a modified  $p_{valid}$ , which accounts for the imbalanced number of target classes. For each sector  $s_i$  with  $k$  target classes, we used Equation 7 to compute a vector of corresponding weight factors,  $r_{s_i}^h$  to be multiplied to each  $p_{valid}$  from Equation 6.

$$r_{s_i}^h = \frac{|M_i|}{k \times |C_{s_i}^h|} \quad (7)$$

where  $|C_{s_i}^h|$  is the number of grid pixels under a given target class or cluster  $h$ .

Table 2: Comparison of the total buildings, dwellings, and occupants among DeepC4, GEM, and METEOR. The percentage values inside the parentheses indicate the accuracy in percentage errors with respect to the census records.

Counts	Census	DeepC4	GEM	METEOR
Building	-	3,200,582	3,258,527	3,368,644
Dwelling	3,312,743	<b>3,350,277 (1.13%)</b>	3,379,883 (2.03%)	-
Occupant	13,100,600	<b>13,246,394 (1.11%)</b>	13,531,804 (3.29%)	-

Table 3: Comparison of the total buildings, dwellings, and occupants in urban and rural settlements between DeepC4 and GEM. The percentage values inside the parentheses indicate the accuracy in percentage errors with respect to the census records.

	Census		DeepC4		GEM	
	Rural	Urban	Rural	Urban	Rural	Urban
Building	-	-	2,270,418	929,866	2,448,058	810,469
Dwelling	2,348,456	964,287	<b>2,368,775 (0.87%)</b>	<b>981,502 (1.8%)</b>	2,536,213 (8%)	843,670 (-13%)
Occupant	9,545,149	3,701,245	<b>9,545,149 (0%)</b>	<b>3,701,245 (0%)</b>	10,075,690 (5.6%)	3,456,114 (-7%)

Table 4: Comparison of the total buildings for each general macro-taxonomy class among DeepC4, GEM, and METEOR.

Description	DeepC4 (A)	GEM (B)	METEOR (C)	A vs C	B vs C	A vs B
All	3,200,582	3,258,527	3,368,644	5.1%	3.3%	<b>1.8%</b>
Sundried blocks	1,594,922	1,340,170	1,813,852	<b>13%</b>	30%	17%
Reinforced concrete	20,017	16,920	32,158	47%	62%	<b>17%</b>
Informal	4,470	24,061	27,228	144%	<b>12%</b>	137%
Rubble stone	18,672	8,563	27,697	<b>39%</b>	106%	74%
Concrete block	15,935	19,769	58,281	114%	99%	<b>21%</b>
Brick masonry	665,498	545,573	126,049	136%	125%	<b>20%</b>
Wood	24,393	22,736	28,832	17%	24%	<b>7%</b>
Wattle and daub	856,675	1,280,734	1,254,547	38%	<b>2.1%</b>	40%

## 4. Results and Discussion

### 4.1. Comparing DeepC4, METEOR, and GEM

Comprehensively comparing the outputs of DeepC4, METEOR, and GEM and disentangling the benefits of using DeepC4 and improved fine-grained inputs (e.g., average household size for urban and rural areas) are challenging and non-trivial because of the closed-source information on the methodological implementation of past studies and their original input data. Thus, in the succeeding discussions, the basis of our comparative analyses and discussions are the resulting outputs as compared to the available 2022 census-based aggregated information in Table 2, Table 3, and Table 6. In addition, because of the absence and inherent difficulty to maintain groundtruth information for other inferred outputs such as the distributions of general macro-taxonomy classes and height categories at the national level, we instead calculated pairwise percent differences to assess inter-model agreement among the outputs of DeepC4, METEOR, and GEM in Table 4 and Table 5.

Another key challenge is the temporal inconsistency among the outputs of DeepC4, METEOR, and GEM. Thus, we uniformly scaled up the outputs of METEOR and GEM using the multipliers, 1.37 and 1.05, to convert from 2012 and 2020, respectively, to 2022. These multipliers are based on the assumptions that the outputs of METEOR used the 2012 dwelling counts from the available census records during its time of analysis and that the outputs of GEM derived a 50-year

linear trend for building counts. Although such a simple projection approach can further propagate uncertainties, the corresponding converted outputs of METEOR and GEM were found to be comparable, with the smallest possible percentage differences, confirming that these assumptions can be used reliably. We also compare the outputs of DeepC4 with those of METEOR and GEM in terms of their respective numerical estimates by urban morphology indicators and the quality of their spatial disaggregation, and discuss their respective accuracies, for cases wherein census records are available.

#### 4.1.1. By building, dwelling, and occupant counts

At the national level, our findings in Table 2 show that the numbers of dwellings and occupants of the outputs of DeepC4 have higher accuracy with percentage errors of 1.13% and 1.11% than those of GEM with percentage errors of 2.03% and 3.29%, respectively. For the number of buildings, the outputs of DeepC4 also reveal increasing differences with those of GEM (~58k more) and METEOR (~168k more), which also follows that the corresponding numbers of dwellings and occupants of METEOR will have the lowest accuracy than those of DeepC4 and GEM. While the linear scaling between two temporal periods of measurement could provide a possible projection of the trend in the number of buildings, our results imply that the Rwandan urban development through the years may have followed a more complex dynamics, indicating that linear scaling may lead to an overestimation of the number of

Table 5: Comparison of the total buildings for each height category between DeepC4 and GEM.

Class	DeepC4	GEM	% Difference
All	3,200,284	3,258,527	1.8%
H:1	1,776,985	1,927,411	6.9%
H:2	1,397,280	1,312,061	4.7%
H:3	10,380	6,825	17%
HBET:3-6	15,276	12,048	18%
HBET:4-7	291	144	23%
HBET:8+	73	38	13%

buildings, dwellings, and occupants.

When classified into settlement types, in Table 3, the numbers of rural and urban dwellings of the outputs of DeepC4 result in percentage errors of 0.87% and 1.8%, respectively, whereas those of GEM overestimate the rural dwelling by 8% and underestimate the urban dwelling by 13%. Similarly, both rural and urban occupants considered by the DeepC4 perfectly matches the official census records whereas those of GEM respectively deviated by 5.6% and -7%. Considering the number of buildings, the outputs of DeepC4 estimated ~178k fewer rural buildings and ~119k more urban buildings.

This signifies the value of a more fine-grained census statistics at the level of sectors, effectively reducing the resulting uncertainty across resolutions, compared to GEM which used a single average household size for the urban and rural areas of the entire Rwanda and five rows of data on population counts at the provincial level (Paul et al., 2022). In addition, these findings also underscore the effect of the selection of the average household size at different levels of aggregation on the reliability and uncertainty of the resulting large-scale exposure and risk outputs, which have been shown to be important in characterizing the urban-rural divide and its relative regional degrees of physical vulnerability for any subsequent risk calculation.

#### 4.1.2. By urban morphology indicators

Due to their respective inherent modelling differences, it is difficult to perform a perfect one-to-one similarity on the inferred distribution of urban morphology among DeepC4, METEOR, and GEM. Thus, instead, we provide a weak comparison on the general groups of macro-taxonomy classes in Table 4 using the assumed relationships in Appendix Appendix B. In Table 5, we also present a comparison of the distribution of the classes of building height between DeepC4 and GEM to demonstrate the incorporation of expert belief system on both approaches.

In Table 4, while the total buildings across all general groups of macro-taxonomy classes observe minimal percentage differences of 1.8% to 5.1%, DeepC4 and GEM, on one hand, share a closer agreement for reinforced concrete, concrete block, brick masonry, and wood. On the other hand, DeepC4 and METEOR have more precise estimates for sundried blocks and rubble stones whereas, only under the

categories of informal and wattle-and-daub, DeepC4 is less favorable when compared to GEM and METEOR.

Despite the absence of building-level information to validate this distribution of macro-taxonomy classes, our results still highlight the observed sensitivity on the possible composition of macro-taxonomy classes of the building stock at a large scale using various approaches. Nevertheless, Table 4 show that outputs of DeepC4 and GEM have a more similar underlying expert belief system, except for the 'informal' category, which can be attributed to the overlapping with other macro-taxonomy classes and the use of sector-level rural and urban household sizes, significantly affecting the allocation of the number of buildings under the said category in DeepC4.

For the inferred distribution of building heights between DeepC4 and GEM, Table 5 shows that the more discrete height categories (i.e., H:1, H:2, and HBET:8+) achieve the lowest percentage differences up to 13%, while the categories of building heights with overlapping ranges (i.e., H:3, HBET:3-6, and HBET:4-7) have higher percentage differences up to 23%. When combined, the group of H:3, HBET:3-6, and HBET:4-7 corresponds to a total percentage difference of 31%, with DeepC4 estimating 6,930 more buildings. In addition, DeepC4 has higher estimates for taller buildings (i.e., H:2, H:3, HBET:3-6, and HBET:4-7) while GEM has only higher estimates for H:1.

While DeepC4 incorporated the weak supervision from the available building-level height information from Bachofer et al. (2019), these results also reflect the uncertainty in associating lower and upper bounds of building heights with a specific number of floor levels, as shown in Table B.2 in Appendix B. For example, H:1 may likely correspond to a building height of 3 meters, but, due to the uniqueness of the different wall types and macro-taxonomy classes, it can be possibly lower for the case of many informal settlements with weak structural integrity and higher for the case of more improved structural designs of buildings, such as reinforced concrete.

Our results, however, provide an alternative distribution of building height classes that is both based on the expert belief system also used in Paul et al. (2022) and an extended benchmarking from the use of weak supervision from the available groundtruth data from Bachofer et al. (2019). Overall, we note that integrating expert belief systems (e.g., local understanding of the number of floor levels) and observational data (e.g., mapped building heights in meters) is a key challenge in characterizing the regional urban morphology for disaster risk assessment.

#### 4.1.3. By spatial disaggregation quality

Because of the differences in spatial resolutions of aggregation, we present two comparative analyses: Figure 3 shows a map and histogram of percentage differences between DeepC4 and METEOR at the 500-meter pixel; and Table 6 presents percentage differences on the number of dwellings considered by DeepC4 and GEM and their corresponding accuracy in percentage errors with respect to the official census records at the province level.

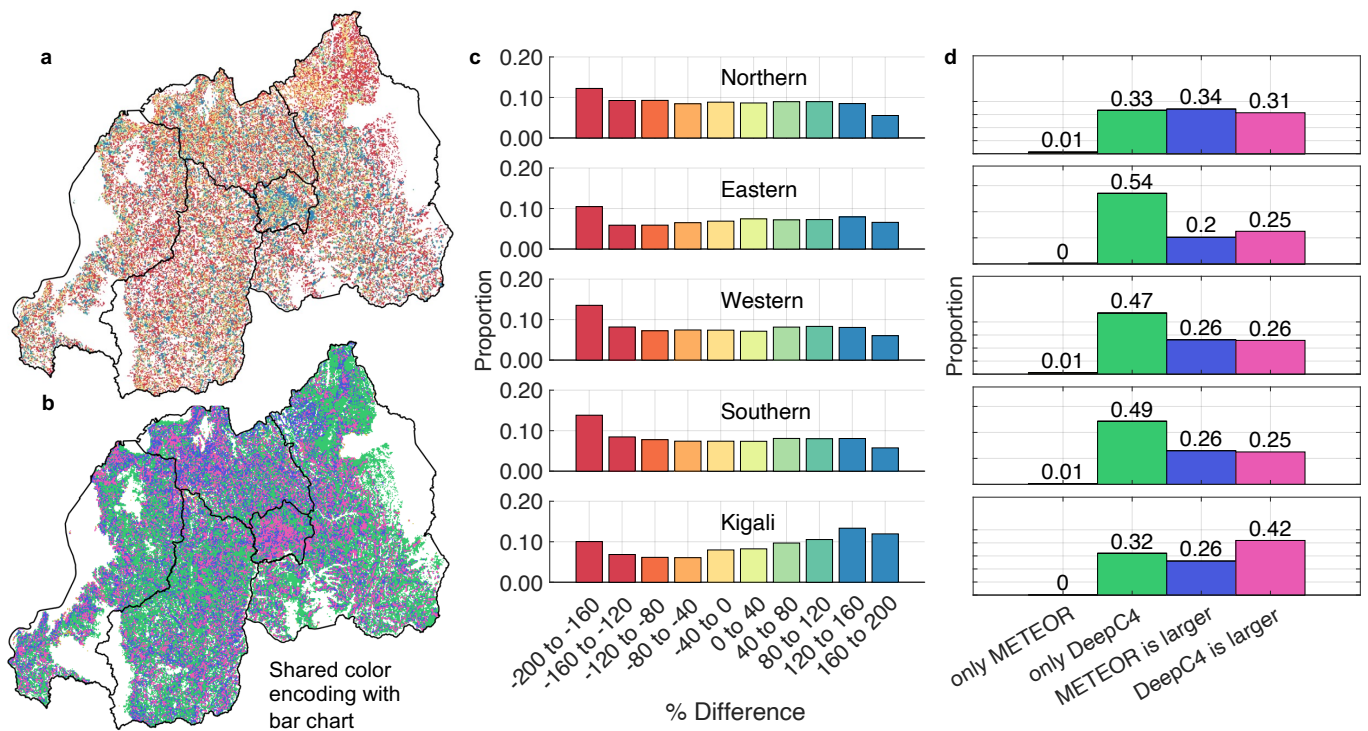


Figure 3: Comparison of the spatial disaggregation between DeepC4 and METEOR at 500-meter pixel. Calculated percentage differences (a) visualized on a map and (c) expressed as a histogram chart showing the proportion of pixels per province. Positive percentage differences indicate that outputs of DeepC4 are larger than those of METEOR and negative otherwise. Categorical difference as (b) a map and (d) a histogram chart showing the proportion of pixels for each descriptive category. The color encoding of map and bar chart is shared between (a) and (c), and between (b) and (d).

Table 6: Comparison of the spatial disaggregation between DeepC4 and GEM at the province level. For each province, this shows the number of urban, rural, and total dwellings. The percentage values inside the parentheses indicate the accuracy with respect to the census records.

Dwelling	Province	Census	DeepC4	GEM	% Difference
Total	North	506,064	<b>509,744 (0.7%)</b>	483,807 (-4.4%)	5.22%
	East	886,132	<b>896,945 (1.2%)</b>	950,320 (7.2%)	5.78%
	West	671,506	<b>677,394 (0.9%)</b>	733,609 (9.2%)	7.97%
	South	760,173	<b>770,372 (1.3%)</b>	790,089 (3.9%)	2.53%
	Kigali	488,868	<b>495,822 (1.4%)</b>	422,058 (-14%)	16.07%
Rural	North	417,670	<b>419,807 (0.5%)</b>	403,373 (-3.4%)	3.99%
	East	700,049	<b>705,767 (0.8%)</b>	792,306 (13%)	11.55%
	West	522,847	<b>527,834 (1.0%)</b>	611,632 (17%)	14.71%
	South	651,454	<b>654,395 (0.5%)</b>	658,727 (1.1%)	0.66%
	Kigali	56,436	<b>60,973 (8.0%)</b>	70,176 (24%)	14.03%
Urban	North	88,394	<b>89,937 (1.7%)</b>	80,434 (-9.0%)	11.16%
	East	186,083	<b>191,178 (2.7%)</b>	158,014 (-15%)	18.99%
	West	148,659	<b>149,560 (0.6%)</b>	121,977 (-18%)	20.32%
	South	108,719	<b>115,978 (6.7%)</b>	131,362 (21%)	12.44%
	Kigali	432,432	<b>434,849 (0.6%)</b>	351,882 (-19%)	21.09%

Although METEOR estimated  $\sim 168k$  more buildings, Figure 3b and 3d show that outputs of DeepC4 occupy more 500-meter grid pixels by 32% (Kigali City) to 49% (Southern Province), which is indicative of the urban development captured by the EO data for the year 2022. While METEOR estimates a slightly higher number of buildings in 34% of all grid pixels in the Northern Province, the general trend across all provinces in DeepC4 still shows that 25% of all grid pixels in Eastern and Southern Provinces to 42% for Kigali City have more building counts than METEOR.

It is important to note that Figure 3b and 3d illustrate only the differences on the space or grid pixels with which either DeepC4 or METEOR has disaggregated values, regardless of the magnitude of their differences. However, these results emphasize that the quality of large-scale exposure datasets also concerns not only the numerical accuracy of the disaggregated building counts but also the spatial accuracy as to where these buildings are located on the map, signifying the critical influence of urban dynamics and temporal consistency of EO data on their degrees of exposure to natural hazards.

Furthermore, in terms of the magnitude of differences between DeepC4 and METEOR, Figure 3c shows that DeepC4 and METEOR result in uniformly distributed percentage differences. However, towards the left end or colored red in Figure 3c, it also indicates that the outputs of METEOR are significantly higher than those of DeepC4 for all surrounding and larger provinces except Kigali City, despite METEOR occupies less grid pixels than DeepC4 in the previous discussion of Figure 3d. Figure 3a also confirms that the province of Kigali City has more grid pixels that are colored blue or higher building counts from DeepC4, which is equivalent to the observed distribution of positive percentage differences in Figure 3c.

These results imply that both the size or areal extent and the relative location (i.e., whether the region is located in the center or perimeter) affect the quality of spatial disaggregation. Particularly, the large areal extents of Northern, Eastern, Western, and Southern Provinces provide more possible and uncertain locations for disaggregation, while the province of Kigali City with the lowest areal extent at the center has limited and constrained locations, resulting in the lowest categorical difference at 32% where an estimate of DeepC4 exists in Figure 3d.

In Table 6, even at the province level, DeepC4 appears to have a set of more accurate numbers of dwellings for both urban and rural areas than those of GEM. For urban dwellings, GEM underestimates by 9% to 19% for all provinces except the South Province, which observes a large overestimation by 21%. For rural dwellings, GEM significantly overestimates Kigali City by 24%, followed by the East and West Provinces by 13% and 17%, respectively. Nevertheless, GEM achieves the most accurate numbers for rural dwellings for the North and South provinces, which are also the most precise estimates with the least percentage differences at 3.99% and 0.66%, respectively, when compared with the outputs of DeepC4.

Our results show that constraining the spatial disaggregation by incorporating census statistics and encoding expert belief

systems in a form of probabilistic relationships among various urban morphology indicators has effectively established a consensus while learning efficient reduced-dimension representations that are able to cluster under weak supervision of available building-level groundtruth information and infer the distribution of the characteristics of the urban layout.

#### 4.2. Assessing Overall Predictive Performance

To understand the reliability of the learning capability and predictive performance of our trained DeepC4 model, we present the learning curves in Figure 4 with an example set of prediction and  $p_{valid}$  maps in Figure 5 on the use of weak supervision of partially available building-level groundtruth of Bachofer et al. (2019).

In Figure 4a and 4b, our trained DeepC4 model has converged to a set of stable reduced-dimension latent representations, resulting in a mean-squared error of 0.66 (a 44% reduction from the initially calculated reconstruction loss) and a Euclidean distance-based prediction loss of 3.376 (a measurable 5.4% reduction from the initially calculated prediction loss). During the initial training phase, the reconstruction and clustering losses were of comparable orders of magnitude and converged to stable values. Consequently, the current unweighted formulation is sufficient to jointly achieve reconstruction quality and the learning of a meaningful reduced-dimensional latent representation within the proposed framework.

In addition, the observed fluctuation trends of prediction loss in Figure 4b, which are more pronounced than those of the reconstruction loss in Figure 4a, can be attributed to the varying sizes and non-uniform clustering behavior of sectors with different proportions of clusters. In contrast, the smoother curve of reconstruction loss is inherent to the spatially continuous structure of EO satellite imagery signals, which vary gradually across neighboring pixels. The reconstruction loss curve continues to decline minimally beyond the optimal epoch at 184 but the prediction loss curve starts to increase, which implies that an optimal reconstruction quality has been achieved already and any further iteration on the reconstruction would only result in a set of learned latent representations that are too sensitive to a deviating clustering behavior.

Furthermore, our results in Figure 4c, 4d, and 4e show that, even at the initial clustering implementation, the incorporation of constraints has already enabled a desirable performance with respect to the cluster-level sizes, as indicated by the  $p_{valid}$  respectively starting at 98.97%, 96.64%, and 95.34% and optimized at 99.03%, 96.45%, and 95.87% for roof, wall, and height. As the joint multitask learning continues, the trade-off exhibits an increasing trend in Figure 4c for roof, an increasing-to-decreasing trend in Figure 4d for wall, and an increasing-to-constant trend in Figure 4e for height.

These reported high performances across all tasks are consistent with the observed high degree of class imbalance, in which a small number of classes dominate the majority of grid pixels, as previously indicated in Table 5, in addition to the influence of the mapping scheme of shared and overlapping

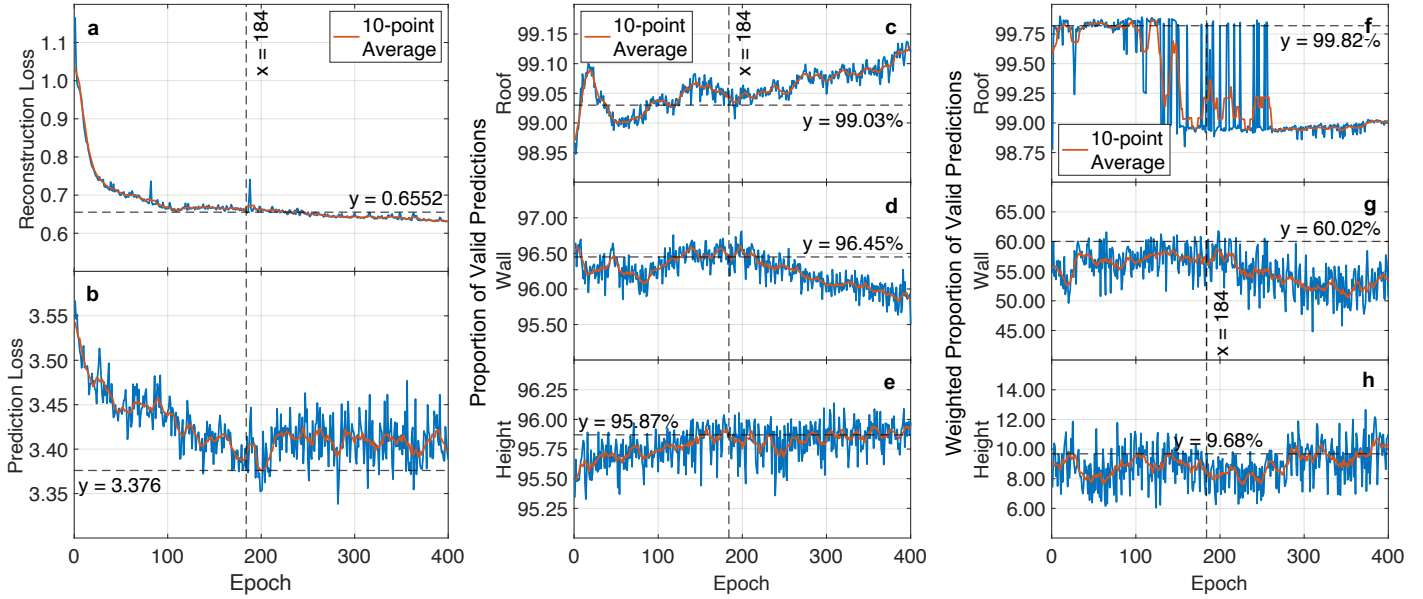


Figure 4: Learning curves. **(a)** reconstruction loss (i.e., how effective the autoencoder is in reducing the high-dimensionality into a meaningful reduced-dimension representations); **(b)** prediction loss (i.e., how accurate the resulting reduced-dimension representations are with respect to available building groundtruth info); **(c-e)** absolute  $p_{valid}$  for each prediction task (roof, wall, and height); and **(f-h)** similar plots but accounting for the imbalanced number of target classes.

characteristics between the building-level groundtruth information and desired indicators of urban morphology. Accordingly, this explains the use of a modified  $p_{valid}$  considering such class imbalance, as emphasized in Equation 7, to more appropriately evaluate the overall predictive performance in Figure 4f, 4g, and 4h.

In the same way, evaluating the  $p_{valid}$  while accounting for the imbalanced number of target classes resulted in a similar behavior, particularly for the wall and height, respectively in Figure 4g and 4h. However, Figure 4f shows that, in the earlier part of the joint multitask training, it achieves a more optimal performance and tends to become constant in the later part, which, in Figure 4c, still indicates an increasing absolute  $p_{valid}$ .

In addition, the magnitude of the weighted  $p_{valid}$  in Figure 4g being higher than that of Figure 4c reflects the large difference in cluster sizes among roof classes. Similarly, Figure 4g and 4h having lower magnitudes than those of Figure 4d and 4e respectively suggests that the number of wall and height classes may be limited and overlapping, despite our efforts in linking different classifications between Bachofer et al. (2019) and the classes in Table 1. This implies that the optimality based on the imbalanced number of target classes and different standards for target classes, which is common in an urban morphology disaggregation task with overly dominating group of classes, is an important consideration in spatial disaggregation. Nevertheless, even though the partially available building-level groundtruth provides limited or weak supervision, the results of our 5-fold cross-validation implementation show a drop across all metrics by only 2%.

To visualize these metrics on the map, Figure 5a to 5d show

a set of prediction maps for the distribution of roof, wall, height, and macro-taxonomy classes over a few sectors in Kigali City, as labeled in Figure 5h and referenced in Figure 5l. Using the available building-level groundtruth information from which we trained our model using their calculated losses, Figure 5e to 5g shows that most grid pixels are accurately predicted (i.e., valid predictions in colored green) for maps of roof, wall, and height. Presenting these pixel maps as sector-level summaries in Figure 5i to 5k, our results also confirm that our trained DeepC4 model achieved a desirably improved performance with the clustering task for roof and height classes being notably more precise compared to that for wall.

#### 4.3. Mapping Rwandan Urban Morphology

Figure 6 summarizes the resulting prediction pixel maps into pie charts aggregated at the province, district, and sector levels. While the charts for roof and wall merely reflect the proportion dictated by the official census records because the clustering occurs at the sector level, DeepC4 gives additional significant insights into the consistency of the quality of constraints for roof and wall and the distribution of height and macro-taxonomy class and extends the approach of the METEOR and GEM by performing a fine-grained implementation using the information derived from various EO signals and weakly supervised by the available building-level groundtruth data.

Figure 6a shows that roofs made of tiles are more prominent in western Rwanda whereas iron sheet is the most commonly used roof material in eastern Rwanda. At the district level, we see in Figure 6e that tiles are more common in the Southern

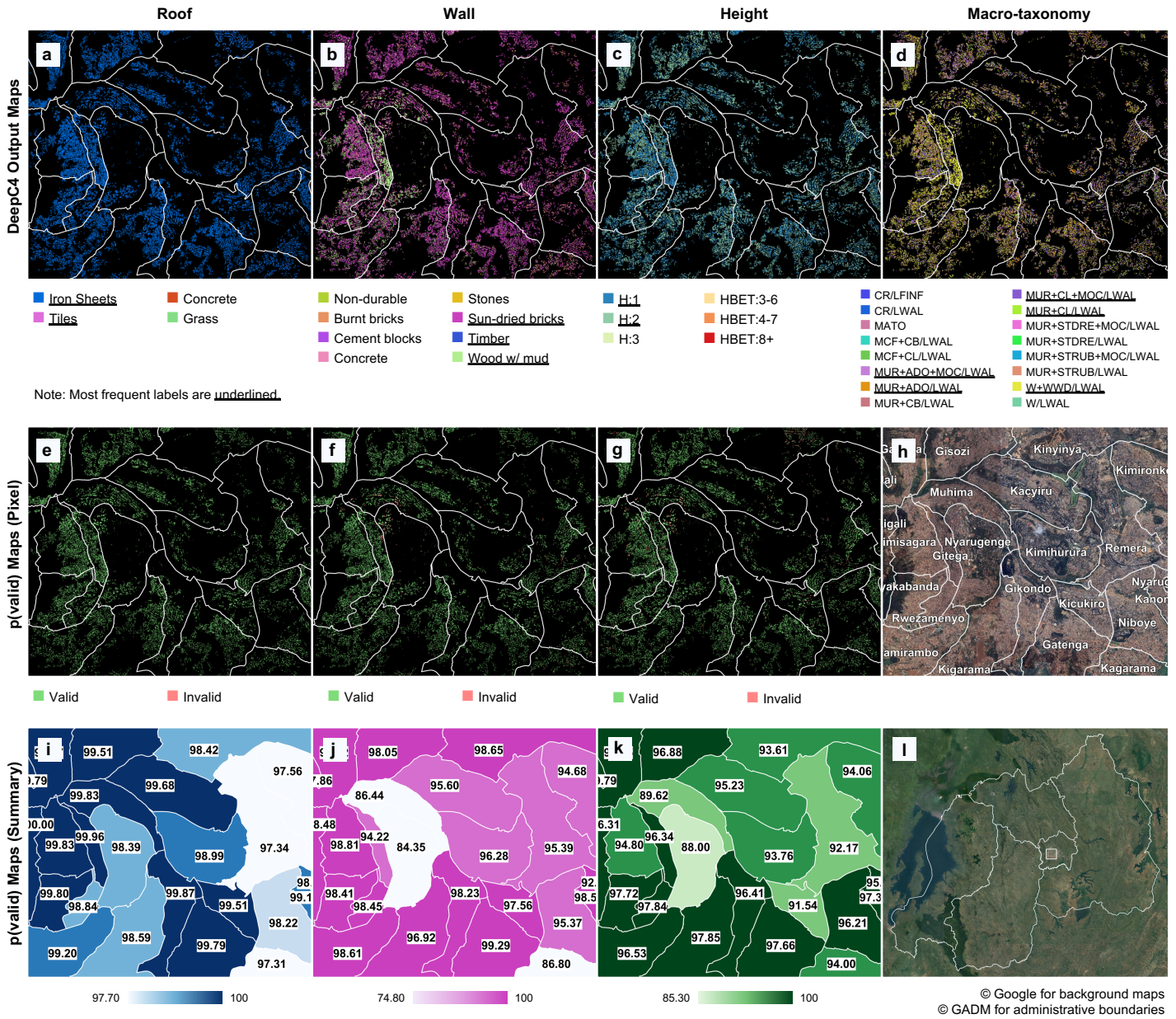


Figure 5: Usefulness of partially available building-level groundtruth. (a-d) a set of prediction maps as a result of DeepC4; (e-g) corresponding  $p_{valid}$  maps; (h) reference background map with sector labels; (i-k) aggregated sector-level values of  $p_{valid}$  maps; and (l) reference location.

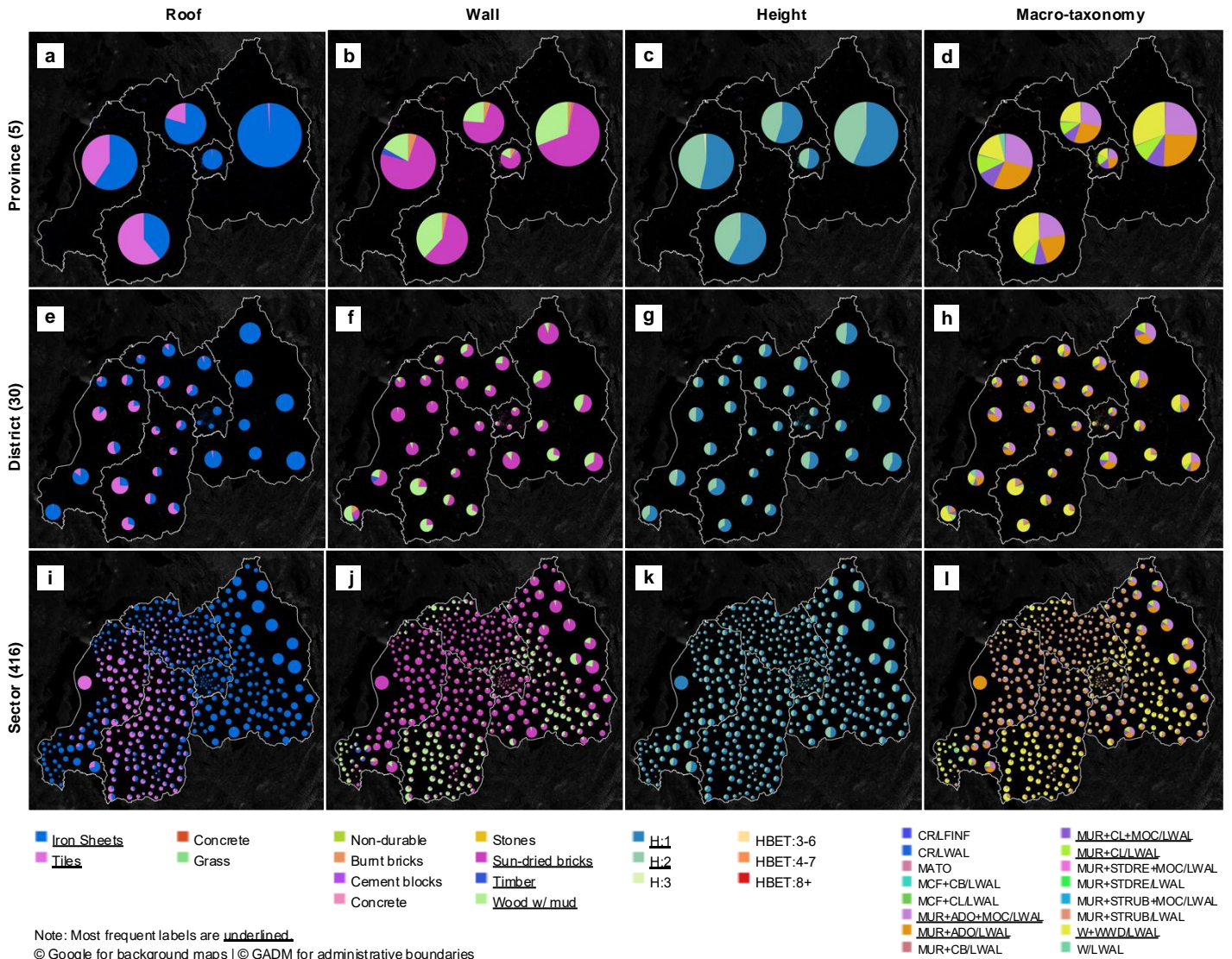


Figure 6: Summary diagrams of the number of buildings for each urban morphology indicator (roof, wall, height, and macro-taxonomy classification, respectively from left to right) at the: (a-d) province, (e-h) district, and (i-l) sector level

Province and on the northern portion of the Western Province. At the sector level in Figure 6i, the use of iron sheets evidently dominates the Eastern Province and Kigali City, including the southern part of the Western Province and the perimeter to the north of the Northern Province.

Figure 6b shows that the majority of wall material is sun-dried bricks, followed by wood with mud. At the district level in Figure 6f, we see that walls made of wood with mud take a significant proportion in the southern parts of the Western and Southern Provinces. Walls made of timber also remain prominent in the southern parts of the Western Province. Towards the center near Kigali City, we see a pattern in which sun-dried brick has become the major wall material. At the sector level in Figure 6j, the Western Province has more sun-dried brick in its central and northern parts, followed by wood with mud in the southern parts, with a minor proportion of timber-made walls in a few sectors. The Northern and

Southern provinces share a similar pattern wherein the outer perimeter is dominated by wood-with-mud-made walls and the sun-dried bricks are concentrated towards the center near Kigali City. In Kigali City, we see the sun-dried brick is the main wall material. For the Eastern province, its southwest and northeast parts are dominated by the sun-dried bricks, with the center concentrated with timber-made walls.

For the height distribution in Figure 6c, 6g, and 6k, we see that the dominant proportion of H:1 is slightly higher than that of H:2. In the southern part of the Southern Province, we see that H:1 is significantly higher than H:2. For the inferred macro-taxonomy distribution in Figure 6d, unreinforced adobe block masonry with cement mortar (MUR+ADO, MUR+ADO+MOC) and wattle and daub (W+WWD) are the main macro-taxonomy classes, followed by unreinforced clay brick masonry with cement mortar (MUR+CL, MUR+CL+MOC). At the district and sector levels in

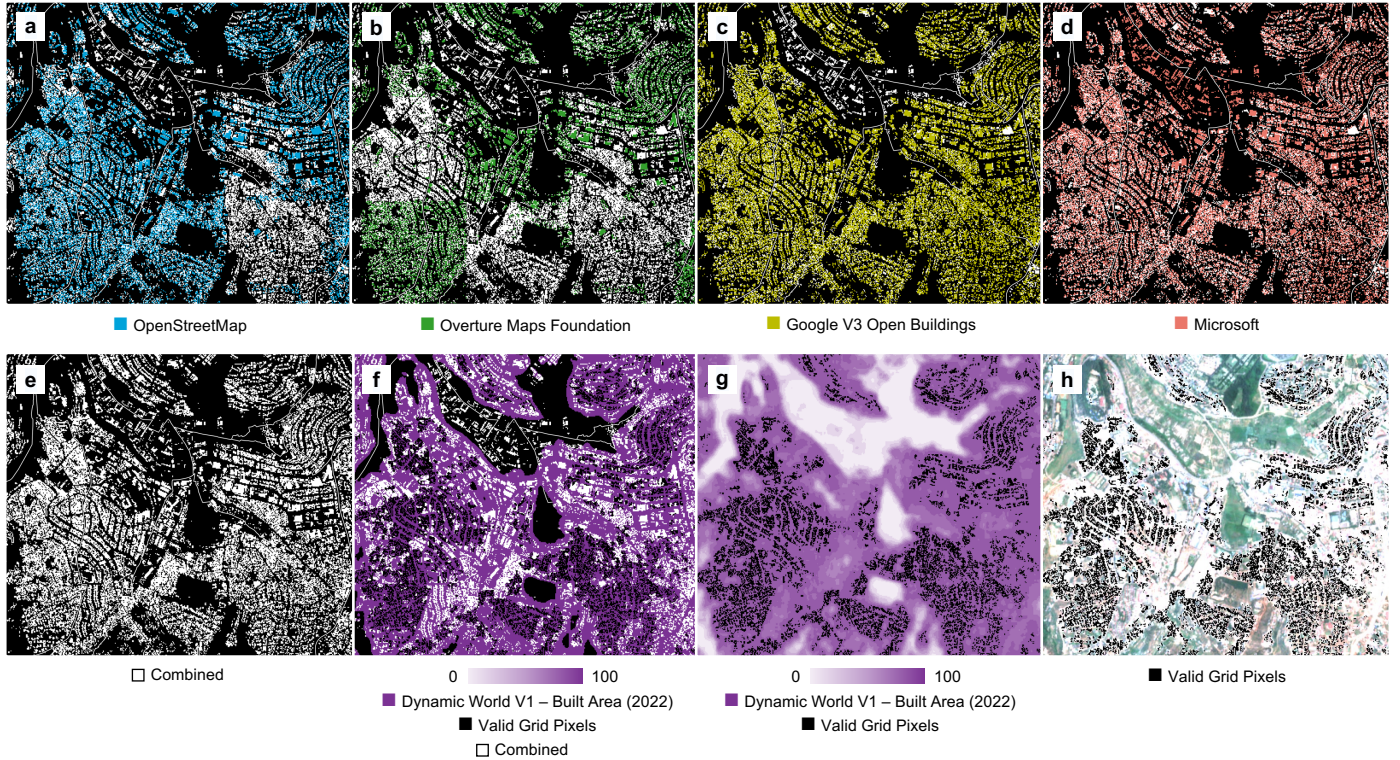


Figure 7: Comparison of built area information. (a-e) various imperfect building footprint sources and (f-g) the use of Dynamic World V1 near-real-time land use land cover as additional information for (h) possible building locations for subsequent clustering implementation of DeepC4.

Figure 6h and 6l, respectively, we see the W+WWD are more prominent in the southern part of the Southern Province and the center of the Eastern Province. For the northern part of the Eastern and Southern Province and the southern part of the Northern Province, we see that MUR+ADO and MUR+ADO+MOC are the main macro-taxonomy classes.

The spatial distribution of our resulting Rwandan urban morphology relies on the use of many imperfect representations of the building footprint, as shown in Figure 7a to 7d. In the provided example in Figure 7, OpenStreetMap and Overture did not have building footprints on the southeastern part of the illustration. Google V3 was also not able to map the building footprints in the northern part. Among them, Microsoft seems to provide most of the building footprints combined from all four sources (see Figure 7e). Considering these four imperfect sources to be equally imperfect due to their lack of temporal definition, the probability values from the Dynamic World V1 Built Area validated and finalized a set of building footprint pixels (see Figure 7f and 7g) which also closely resembles the Sentinel-2 RGB imagery in Figure 7h.

## 5. Conclusion and Future Work

Our proposed novel DeepC4, a deep constrained clustering model, advances the existing classical spatial disaggregation techniques using deep learning and EO data to understand the

distribution of various urban morphology characteristics at large scales. Using cluster-level constraints, multitask optimization, and multilabel conditionality, we specifically demonstrated a deep learning model that can uniquely cope with the challenges of weak supervision when inferring the Rwandan urban morphology, in terms of indicators often used in the practice of disaster risk assessment. By considering the explicit importance of well-validated census and experts' belief systems, our approach also contributes to the overall consistency of resulting deep learning-based maps, thereby improving their relative explainability and interpretability with respect to the current understanding of end users. Using several built environment data and partially available building-level groundtruth, our work has also significantly contributed new insights into the existing Rwandan exposure and physical vulnerability of GEM and METEOR towards a spatial auditing of existing coarse-grained derived information.

For future work, we recommend extending this study with temporal variables to understand the evolution of urban morphology. We also recommend investigating other regions with higher diversity and uniformity across labels to assess the training quality and sensitivity.

## Data and Code Availability

The 9.2GB-data and code are respectively available in our publicly available Zenodo (<https://doi.org/10.5281/ze>

[zenodo.13119552](https://zenodo.org/record/13119552)) (Dimasaka, 2024a) and GitHub repositories (<https://github.com/riskaudit/DeepC4>) (Dimasaka, 2024b).

## Acknowledgment

This work is funded by the UKRI Centre for Doctoral Training in Application of Artificial Intelligence to the study of Environmental Risks (AI4ER) (EP/S022961/1) and the Helmholtz Information & Data Science Academy (HIDA) for providing financial support, enabling a short-term research stay at the Earth Observation Center in the German Aerospace Center to develop the DeepC4. We also acknowledge the GEM Foundation, through Andrés Abarca and Vitor Silva, for the subset of the Global Exposure Model (v2023.1.0) for research purposes. We also appreciate the initial guidance and correspondence from Charles Huyck of the METEOR project and Nicole Paul of the Uniform Africa Exposure Dataset at the outset of this research project.

## References

- Bachofer, F., Braun, A., Adamietz, F., Murray, S., d'Angelo, P., Kyazze, E., Mumuhire, A.P., Bower, J., 2019. Building stock and building typology of kigali, rwanda. *Data* 4, 105.
- Blei, A.M., Angel, S., Civco, D.L., Liu, Y., Zhang, X., 2018. Accuracy assessment and map comparisons for monitoring urban expansion: the atlas of urban expansion and the global human settlement layer. Lincoln Institute of Land Policy: Cambridge, MA, USA .
- Bradley, P.S., Bennett, K.P., Demiriz, A., 2000. Constrained k-means clustering. *Microsoft Research, Redmond* 20, 0.
- Braun, A., Warth, G., Bachofer, F., Hochschild, V., 2019. Identification of roof materials in high-resolution multispectral images for urban planning and monitoring, pp. 1–4. doi:10.1109/JURSE.2019.8809026.
- Brown, C.F., Brumby, S.P., Guzder-Williams, B., Birch, T., Hyde, S.B., Mazzariello, J., Czerwinski, W., Pasquarella, V.J., Haertel, R., Ilyushchenko, S., et al., 2022. Dynamic world, near real-time global 10 m land use land cover mapping. *Scientific Data* 9, 251.
- Brzev, S., Scawthorn, C., Charleson, A.W., Allen, L., Greene, M., Jaiswal, K., Silva, V., 2013. GEM building taxonomy (Version 2.0). Technical Report. GEM Foundation.
- Clark, C.N., Bedada, A., Huff, B., Lita, B., Newbury, A.B., Pacifici, F., 2023. Investigating the resolution-performance trade-off of object detection models in support of the sustainable development goals. *IEEE Journal of Selected Topics in Applied Earth Observations and Remote Sensing* 16, 5695–5713.
- Copernicus Sentinel data, 2024a. Harmonized Sentinel-2 MSI: MultiSpectral Instrument, Level-2A. [https://developers.google.com/earth-engine/datasets/catalog/COPERNICUS\\_S2\\_SR\\_HARMONIZED](https://developers.google.com/earth-engine/datasets/catalog/COPERNICUS_S2_SR_HARMONIZED). Accessed: 2024-07-30.
- Copernicus Sentinel data, 2024b. Sentinel-1 SAR GRD: C-band Synthetic Aperture Radar Ground Range Detected, log scaling. [https://developers.google.com/earth-engine/datasets/catalog/COPERNICUS\\_S1\\_GRD](https://developers.google.com/earth-engine/datasets/catalog/COPERNICUS_S1_GRD). Accessed: 2024-07-30.
- Copernicus Sentinel data, 2024c. Sentinel-2: Cloud Probability. [https://developers.google.com/earth-engine/datasets/catalog/COPERNICUS\\_S2\\_CLOUD\\_PROBABILITY](https://developers.google.com/earth-engine/datasets/catalog/COPERNICUS_S2_CLOUD_PROBABILITY). Accessed: 2024-07-30.
- Darin, E., Kuépié, M., Bassinga, H., Boo, G., Tatem, A.J., Reeve, P., 2022. The population seen from space: when satellite images come to the rescue of the census. *Population* 77, 437–464.
- Demiriz, A., Bennett, K.P., Bradley, P.S., 2008. Using assignment constraints to avoid empty clusters in k-means clustering. *Constrained clustering: advances in algorithms, theory, and applications* 201.
- Dimasaka, J., 2024a. Deep Conditional Census-Constrained Clustering (DeepC4) for Large-scale Multi-task Disaggregation of Urban Morphology. URL: <https://doi.org/10.5281/zenodo.13119552>, doi:10.5281/zenodo.13119552.
- Dimasaka, J., 2024b. DeepC4. URL: <https://github.com/riskaudit/DeepC4>.
- Geiß, C., Priesmeier, P., Aravena Pelizari, P., Soto Calderon, A.R., Schoepfer, E., Riedlinger, T., Villar Vega, M., Santa María, H., Gómez Zapata, J.C., Pittore, M., et al., 2023. Benefits of global earth observation missions for disaggregation of exposure data and earthquake loss modeling: evidence from santiago de chile. *Natural Hazards* 119, 779–804.
- Geiß, C., Thoma, M., Taubenböck, H., 2018. Cost-sensitive multitask active learning for characterization of urban environments with remote sensing. *IEEE Geoscience and Remote Sensing Letters* 15, 922–926.
- Geofabrik GmbH, OpenStreetMap Contributors, 2018. OpenStreetMap Data Extracts. URL <https://download.geofabrik.de/>. Accessed: 2024-07-30.
- Gevaert, C.M., Carman, M., Rosman, B., Georgiadou, Y., Soden, R., 2021. Fairness and accountability of ai in disaster risk management: Opportunities and challenges. *Patterns* 2.
- Global Administrative Areas, 2022. GADM database of global administrative areas, version 4.1. <https://gadm.org/maps/NOR.html>. To view a copy of the license of this work, visit <https://gadm.org/license.html>. Accessed: 2024-07-30.

- Gómez Zapata, J.C., Pittore, M., Cotton, F., Lilienkamp, H., Shinde, S., Aguirre, P., Santa María, H., 2022. Epistemic uncertainty of probabilistic building exposure compositions in scenario-based earthquake loss models. *Bulletin of Earthquake Engineering* 20, 2401–2438.
- Gorelick, N., Hancher, M., Dixon, M., Ilyushchenko, S., Thau, D., Moore, R., 2017. Google earth engine: Planetary-scale geospatial analysis for everyone. *Remote Sensing of Environment* URL: <https://doi.org/10.1016/j.rse.2017.06.031>, doi:10.1016/j.rse.2017.06.031.
- Gouveia, F., Silva, V., Lopes, J., Moreira, R.S., Torres, J.M., Simas Guerreiro, M., 2024. Automated identification of building features with deep learning for risk analysis. *Discover Applied Sciences* 6, 466.
- Grünthal, G., 1998. European macroseismic scale 1998 15, 1–97.
- Huangfu, Q., Hall, J.J., 2018. Parallelizing the dual revised simplex method. *Mathematical Programming Computation* 10, 119–142.
- Huyck, C., Hu, Z., Amyx, P., Esquivias, G., Huyck, M., Eguchi, M., 2019. METEOR: exposure data classification, metadata population and confidence assessment. Report M3. 2/P. Technical Report M3. 2/P. British Geological Survey.
- Jaiswal, K., Wald, D., Porter, K., 2010. A global building inventory for earthquake loss estimation and risk management. *Earthquake Spectra* 26, 731–748.
- Kingma, D.P., 2014. Adam: A method for stochastic optimization. arXiv preprint arXiv:1412.6980 .
- Kircher, C.A., Whitman, R.V., Holmes, W.T., 2006. Hazus earthquake loss estimation methods. *Natural Hazards Review* 7, 45–59.
- Koppel, K., Zalite, K., Voormansik, K., Jagdhuber, T., 2017. Sensitivity of sentinel-1 backscatter to characteristics of buildings. *International Journal of Remote Sensing* 38, 6298–6318. doi:10.1080/01431161.2017.1353160.
- Labetski, A., Vitalis, S., Biljecki, F., Arroyo Ohori, K., Stoter, J., 2023. 3d building metrics for urban morphology. *International Journal of Geographical Information Science* 37, 36–67.
- Lafabregue, B., Gañçarski, P., 2025. I-samarah, an incremental constrained clustering applied to remote sensing images. *Neural Computing and Applications* , 1–25.
- Lampert, T., Lafabregue, B., Serrette, N., Vrain, C., Gañçarski, P., et al., 2019. Constrained distance-based clustering for satellite image time-series. *IEEE Journal of Selected Topics in Applied Earth Observations and Remote Sensing* 12, 4606–4621.
- Meinel, G., Hecht, R., Herold, H., 2009. Analyzing building stock using topographic maps and gis. *Building Research & Information* 37, 468–482.
- Microsoft, 2024. Global ML Building Footprints. URL: <https://github.com/microsoft/GlobalMLBuildingFootprints>. Accessed: 2024-07-30.
- National Institute of Statistics Rwanda, 2023. Fifth Population and Housing Census - 2022. <https://www.statistics.gov.rw/datasource/fifth-population-and-housing-census-2022>. This work is licensed under the Norwegian Licence for Creative Commons Attribution 4.0 International License. To view a copy of this license, visit <https://creativecommons.org/licenses/by/4.0/>. Accessed: 2024-07-30.
- Overture Maps Foundation, 2023. Overture Foundation Building Footprints. URL: <https://beta.source.coop/repositories/cholmes/overture>. Accessed: 2024-07-30.
- Paul, N., Silva, V., Amo-Oduro, D., 2022. Development of a uniform exposure model for the african continent for use in disaster risk assessment. *International Journal of Disaster Risk Reduction* 71, 102823.
- Pesaresi, M., Schiavina, M., Politis, P., Freire, S., Krasnodebska, K., Uhl, J.H., Carioli, A., Corbane, C., Dijkstra, L., Florio, P., et al., 2024. Advances on the global human settlement layer by joint assessment of earth observation and population survey data. *International Journal of Digital Earth* 17, 2390454.
- Petrarulo, L., Lyon, A., Paudyal, A., Zakaria, S., Sokile, C., 2022. METEOR: Legacy Evaluation Report M2. 11/P. Technical Report M2. 11/P. British Geological Survey.
- Pittore, M., Haas, M., Megalooikonomou, K.G., 2018. Risk-oriented, bottom-up modeling of building portfolios with faceted taxonomies. *Frontiers in Built Environment* 4, 41.
- Seljom, P., Kvalbein, L., Hellemo, L., Kaut, M., Ortiz, M.M., 2021. Stochastic modelling of variable renewables in long-term energy models: Dataset, scenario generation & quality of results. *Energy* 236, 121415.
- Silva, V., Sousa, R., Ribeiro Gouveia, F., Lopes, J., Guerreiro, M.J., 2024. A building imagery database for the calibration of machine learning algorithms. *Earthquake Spectra* 40, 1577–1590.
- Sirko, W., Kashubin, S., Ritter, M., Annkah, A., Bouchareb, Y.S.E., Dauphin, Y., Keyzers, D., Neumann, M., Cisse, M., Quinn, J., 2021. Continental-scale building detection from high resolution satellite imagery. arXiv preprint arXiv:2107.12283 URL: <https://beta.source.coop/repositories/cholmes/google-open-buildings/description/>. Accessed: 2024-07-30.

Stevens, F.R., Gaughan, A.E., Linard, C., Tatem, A.J., 2015. Disaggregating census data for population mapping using random forests with remotely-sensed and ancillary data. *PLoS one* 10, e0107042.

Tatem, A.J., 2017. Worldpop, open data for spatial demography. *Scientific data* 4, 1–4.

UN, 2015. Resolution A/RES/70/1. Transforming Our World, the 2030 Agenda for Sustainable Development. Technical Report. United Nations.

United Nations (UN), 2015. Sendai Framework for Disaster Risk Reduction 2015–2030. Technical Report. United Nations.

Wagstaff, K., Cardie, C., Rogers, S., Schrödl, S., et al., 2001. Constrained k-means clustering with background knowledge, in: *ICML*, pp. 577–584.

Wardrop, N.A., Jochem, W.C., Bird, T.J., Chamberlain, H.R., Clarke, D., Kerr, D., Bengtsson, L., Juran, S., Seaman, V., Tatem, A.J., 2018. Spatially disaggregated population estimates in the absence of national population and housing census data. *Proceedings of the National Academy of Sciences* 115, 3529–3537.

Zhou, X., Huang, Z., Scheuer, B., Wang, H., Zhou, G., Liu, Y., 2023. High-resolution estimation of building energy consumption at the city level. *Energy* 275, 127476.

Zhu, S., Wang, D., Li, T., 2010. Data clustering with size constraints. *Knowledge-Based Systems* 23, 883–889.

## Appendix A. Discrete conditional probability values among urban morphology indicators

Table A.1: Relationship between wall and macro-taxonomy classes derived from Paul et al. (2022).

Wall	Type	Macro-Taxonomy	Probability
Wood with mud	Urban	W+WWD/LWAL	1
Sun-dried bricks	Urban	MUR+ADO+MOC/LWAL	0.3
Sun-dried bricks	Urban	MUR+CL+MOC/LWAL	0.2
Sun-dried bricks	Urban	MUR+ADO/LWAL	0.3
Sun-dried bricks	Urban	MUR+CL/LWAL	0.2
Others	Urban	MATO	1
Cement blocks	Urban	MUR+CB/LWAL	0.8
Cement blocks	Urban	MCF+CB/LWAL	0.2
Concrete	Urban	CR/LFINF	0.8
Concrete	Urban	CR/LWAL	0.2
Stone	Urban	MUR+STDRE+MOC/LWAL	0.5
Stone	Urban	MUR+STDRE/LWAL	0.5
Timber	Urban	W/LWAL	1
Burnt bricks	Urban	CR/LFINF	0.25
Burnt bricks	Urban	MUR+CL+MOC/LWAL	0.25
Burnt bricks	Urban	MUR+CL/LWAL	0.412
Burnt bricks	Urban	MCF+CL/LWAL	0.088
Wood with mud	Rural	W+WWD/LWAL	1
Sun-dried bricks	Rural	MUR+ADO+MOC/LWAL	0.4
Sun-dried bricks	Rural	MUR+CL+MOC/LWAL	0.1
Sun-dried bricks	Rural	MUR+ADO/LWAL	0.4
Sun-dried bricks	Rural	MUR+CL/LWAL	0.1
Others	Rural	MATO	1
Cement blocks	Rural	MUR+CB/LWAL	1
Concrete	Rural	CR/LFINF	0.5
Concrete	Rural	CR/LWAL	0.5
Stone	Rural	MUR+STRUB+MOC/LWAL	0.5
Stone	Rural	MUR+STRUB/LWAL	0.5
Timber	Rural	W/LWAL	1
Burnt bricks	Rural	MUR+CL+MOC/LWAL	0.5
Burnt bricks	Rural	MUR+CL/LWAL	0.5

Table A.2: Relationship between macro-taxonomy and height classes (Paul et al., 2022).

Macro-Taxonomy	Height	Probability
CR/LFINF	H:1	0.1
CR/LFINF	H:2	0.35
CR/LFINF	H:3	0.35
CR/LFINF	HBET:4-7	0.15
CR/LFINF	HBET:8+	0.05
CR/LWAL	H:1	0.1
CR/LWAL	H:2	0.35
CR/LWAL	H:3	0.35
CR/LWAL	HBET:4-7	0.15
CR/LWAL	HBET:8+	0.05
MATO	H:1	1
MCF+CB/LWAL	H:1	0.45
MCF+CB/LWAL	H:2	0.45
MCF+CB/LWAL	HBET:3-6	0.1
MCF+CL/LWAL	H:1	0.45
MCF+CL/LWAL	H:2	0.45
MCF+CL/LWAL	HBET:3-6	0.1
MUR+ADO+MOC/LWAL	H:1	0.475
MUR+ADO+MOC/LWAL	H:2	0.475
MUR+ADO+MOC/LWAL	HBET:3-6	0.05
MUR+ADO/LWAL	H:1	0.475
MUR+ADO/LWAL	H:2	0.475
MUR+ADO/LWAL	HBET:3-6	0.05
MUR+CB/LWAL	H:1	0.475
MUR+CB/LWAL	H:2	0.475
MUR+CB/LWAL	HBET:3-6	0.05
MUR+CL+MOC/LWAL	H:1	0.475
MUR+CL+MOC/LWAL	H:2	0.475
MUR+CL+MOC/LWAL	HBET:3-6	0.05
MUR+CL/LWAL	H:1	0.475
MUR+CL/LWAL	H:2	0.475
MUR+CL/LWAL	HBET:3-6	0.05
MUR+STDRE+MOC/LWAL	H:1	0.475
MUR+STDRE+MOC/LWAL	H:2	0.475
MUR+STDRE+MOC/LWAL	HBET:3-6	0.05
MUR+STDRE/LWAL	H:1	0.475
MUR+STDRE/LWAL	H:2	0.475
MUR+STDRE/LWAL	HBET:3-6	0.05
MUR+STRUB+MOC/LWAL	H:1	0.475
MUR+STRUB+MOC/LWAL	H:2	0.475
MUR+STRUB+MOC/LWAL	HBET:3-6	0.05
MUR+STRUB/LWAL	H:1	0.475
MUR+STRUB/LWAL	H:2	0.475
MUR+STRUB/LWAL	HBET:3-6	0.05
W+WWD/LWAL	H:1	0.7
W+WWD/LWAL	H:2	0.3
W/LWAL	H:1	0.4
W/LWAL	H:2	0.4
W/LWAL	H:3	0.2

Table A.3: Relationship between height classes and dwellings (Paul et al., 2022).

Height	Type	Probability	Dwellings
H:1	Dwelling-house	1	1
H:2	Dwelling-house	0.95	1
H:2	Townhouse	0.05	2
H:3	Dwelling-house	0.7	1
H:3	Townhouse	0.2	3
H:3	Apartment/Flat	0.1	8
HBET:3-6	Townhouse	0.25	4
HBET:3-6	Apartment/Flat	0.75	12
HBET:4-7	Apartment/Flat	1	12
HBET:8+	Apartment/Flat	1	16

**Appendix B. Mapping scheme between the target urban morphology indicators and the classification of 2015 Rwanda building groundtruth information (Bachofer et al., 2019).**

Table B.1: Assumed relationship between available building type labels ( $Y_{C^h}$ ) and discrete target census roof classes ( $C_{s_i}^h$ ).

Building Type Labels	Target Census Roof Classes			
	Iron Sheets	Local, Industrial, and Asbestos Tiles	Concrete	Grass
Rudimentary, basic or unplanned buildings	✓			✓
Building in block structure or large courtyard buildings	✓			
Bungalow-type buildings	✓	✓		
Villa-type buildings	✓	✓		
Low to mid-rise multi-unit buildings	✓	✓		
High-rise buildings	✓		✓	
Halls	✓			

Table B.2: Assumed relationship between available height labels ( $Y_{C^h}$ ) and discrete target height classes ( $C_{s_i}^h$ ).

Continuous Height Labels in meters	Discrete Target Height Classes					
	H:1	H:2	H:3	HBET:3-6	HBET:4-7	HBET:8+
(0, 6)	✓	✓				
[6, 9)		✓	✓	✓		
[9, 12)			✓	✓	✓	
[12, 21)				✓	✓	
[21, 24)					✓	✓
[24, +∞)						✓

Table B.3: Assumed relationship between available building type labels ( $Y_{C^h}$ ) and discrete target census wall classes ( $C_{s_i}^h$ ).

Building Type Labels	Target Census Wall Classes							
	Others	Burnt bricks	Cement blocks	Concrete	Stones	Sun-dried bricks	Timber	Wood w/ mud
Rudimentary, basic or unplanned buildings	✓	✓	✓	✓	✓	✓	✓	✓
Building in block structure or large courtyard buildings	✓	✓	✓	✓		✓		
Bungalow-type buildings		✓	✓	✓		✓		✓
Villa-type buildings			✓	✓		✓		
Low to mid-rise multi-unit buildings			✓	✓				
High-rise buildings				✓				
Halls		✓	✓	✓		✓		